




RESEARCH ARTICLE

SIMU/Triple star sensors integrated navigation method of HALE UAV based on atmospheric refraction correction

Ziqian Gao,^{1,2}  Haiyong Wang,^{3*} Weihong Wang,^{1,2} and Yuan Xu⁴

¹ School of Automation Science and Electrical Engineering, Beihang University, Beijing, China.

² Science and Technology on Aircraft Control Laboratory, Beihang University, Beijing, China.

³ School of Astronautics, Beihang University, Beijing, China.

⁴ Shandong Institute of Space Electronic Technology, Yantai, China.

*Corresponding author. E-mail: why@buaa.edu.cn

Received: 13 June 2021; **Accepted:** 20 November 2021; **First published online:** 8 February 2022

Keywords: atmospheric refracton; HALE UAV; triple-FOV star sensors; integrated navigation

Abstract

To achieve autonomous all-day flight by high-altitude long-endurance unmanned aerial vehicle (HALE UAV), a new navigation method with deep integration of strapdown inertial measurement unit (SIMU) and triple star sensors based on atmospheric refraction correction is proposed. By analysing the atmospheric refraction model, the stellar azimuth coordinate system is introduced and the coupling relationship between attitude and position is established. Based on the geometric relationship whereby all the stellar azimuth planes intersect on the common zenith direction, the sole celestial navigation system (CNS) method by stellar refraction with triple narrow fields of view (FOVs) is studied and a loss function is built to evaluate the navigation accuracy. Finally, the new SIMU/triple star sensors deep integrated navigation method with refraction correction upgraded from the traditional inertial navigation system (INS)/CNS integrated method can be established. The results of simulations show that the proposed method can effectively restrain navigation error of a HALE UAV in 24 h steady-state cruising in the stratosphere.

1. Introduction

Celestial navigation is an ancient technology which originates from sea voyages. With the development of modern aerospace technology (e.g., the invention of star sensors), the celestial navigation system (CNS) has become increasingly important for autonomous long-endurance flight vehicles. High-precision star sensors can ensure the attitude accuracy for spacecraft in real time, however, for aircraft, atmospheric influence must be considered. The successive atmospheric models established in recent decades, such as the International Standard Atmosphere (ISA) model, the 1976 U.S. Standard Atmospheric model and the NRLMSISE-00 atmospheric model (Honda et al., 2015; Kurzke and Halliwell, 2018), have gradually supplemented or updated the atmospheric properties for related studies, especially in the fields of aerophysics and aerodynamics. Stellar observation, however, is mainly concerned with two aspects: atmospheric background radiation and atmospheric refraction (Wang et al., 2017b).

Atmospheric background radiation is mainly caused by atmospheric scattering. Under the interference of stray light noise, especially in daytime, the star image measured by star sensor will suffer from low centroiding accuracy or even be submerged (Wang et al., 2021b). In response to this problem, short-wave infrared (SWIR) technology was invented, and some star observation strategies as well as image preprocessing algorithms have been studied (Wang et al., 2017b; Wu et al., 2019). Moreover, the hardware upgrade of all-day star sensors with strong detectivity and high precision is of vital

importance. Thus, various research institutes have developed varieties of star sensor models, such as HERO (High Energy Replicated Optics) system by NASA in 2000, BLAST (Balloon-borne Large-Aperture Submillimeter Telescope) system by the University of Pennsylvania in 2005, DayStar system by Microcosm in 2006 and EBEX (E and B Experiment) telescope by JPL in 2012 (Zheng et al., 2020). The BLAST system with field of view (FOV) of $2^\circ \times 2.5^\circ$ can observe fix stars with visual magnitude 9.0 and reach an absolute accuracy within $5''$ in daytime float condition (Rex et al., 2006). The EBEX telescope has an accuracy up to $1.5''$ with the limiting magnitude of roughly 7.0 (Chapman et al., 2015). It can be seen that the application of an all-day star sensor on a balloon-borne platform makes it possible for a high-altitude long-endurance unmanned aerial vehicle (HALE UAV) to utilise the CNS method when cruising in the stratosphere with slow attitude manoeuvres.

Atmospheric refraction is another critical factor that will cause observed deviation, resulting in two issues: influence on star pattern recognition, which can be easily solved in practice (Ho, 2012; Wang et al., 2017a), and the introduction of attitude error as well as position error in further calculation (Wang et al., 2011). Therefore, it is essential to calibrate the refraction model for the specific atmospheric environment (The Purple Mountain Observatory, 2021). Based on the given atmospheric refraction model, Ning and Wang (2013) proposed a method of celestial altitude determination to realise the positioning of a motionless vessel with quite high accuracy under ideal conditions. However, for the manoeuvring UAV in flight, the attitude estimation is rough without horizontal reference, which complicates the problem in positioning by CNS alone. Thus, other navigation systems should be integrated with CNS to meet the demands of engineering applications.

The strapdown inertial navigation system (SINS), as a common use of inertial navigation system, is composed of strapdown inertial measurement unit (SIMU). As a totally autonomous navigation method, it can provide the position, velocity and attitude of the vehicle with high frequency and high accuracy in a short time, despite its accumulation of error in the long run (Qin, 2006). Based on the existing SINS/CNS integrated system, Zhu et al. (2018) proposed an overall optimal correction scheme for UAV integrated navigation. However, this method only applies to near-space vehicles, as aerial vehicles cannot fly high enough to achieve indirect horizon-sensing through the stratosphere. The best scheme to implement the SINS/CNS method for UAV is the deep integrated mode (He et al., 2014; Ning et al., 2018).

So far, the correlational studies have mainly focused on the calibration of the atmospheric model, the improvement of star sensor performance and the optimisation of the SINS/CNS integrated algorithm. Nevertheless, the analytic geometric relationship of navigation parameters under the stellar refraction condition and the corresponding effective all-day navigation algorithm still lack study. On account of this, in this paper the authors propose a novel SIMU/triple star sensor deep integrated navigation method with atmospheric refraction correction which applies to HALE UAV in all-day flight.

The paper is divided into six sections. After this introduction section, the atmospheric refraction model for aircraft is analysed to establish the coupling relationship between parameters of attitude and position in Section 2. Some correlational research on triple-FOV star sensors navigation by stellar refraction is presented in Section 3. In Section 4, a comparison of the SIMU/triple star sensors deep integrated method with refraction corrected and with refraction uncorrected is put forward, and the Kalman filter is designed. Simulation verification and analysis are shown in Section 5 and conclusions are drawn in Section 6.

2. Atmospheric refraction model analysis for aircraft

According to the law of refraction, starlight will be refracted and bent inward to the geocentre when passing through the atmosphere. Therefore the apparent position of a star will be a little higher than its actual one. For the certain position of a UAV, the unit vectors of the stellar apparent direction \mathbf{u}_a and the real direction \mathbf{u}_r (reverse direction of starlight) in geocentric equatorial inertial coordinate system (denoted as frame i), together with the zenith direction ζ are coplanar, which is defined as the stellar azimuth plane μ_a . The angle between \mathbf{u}_a and \mathbf{u}_r is defined as the starlight refraction angle ρ , whose relationship with stellar apparent zenith distance z_a and real zenith distance z_r is shown in Figure 1,

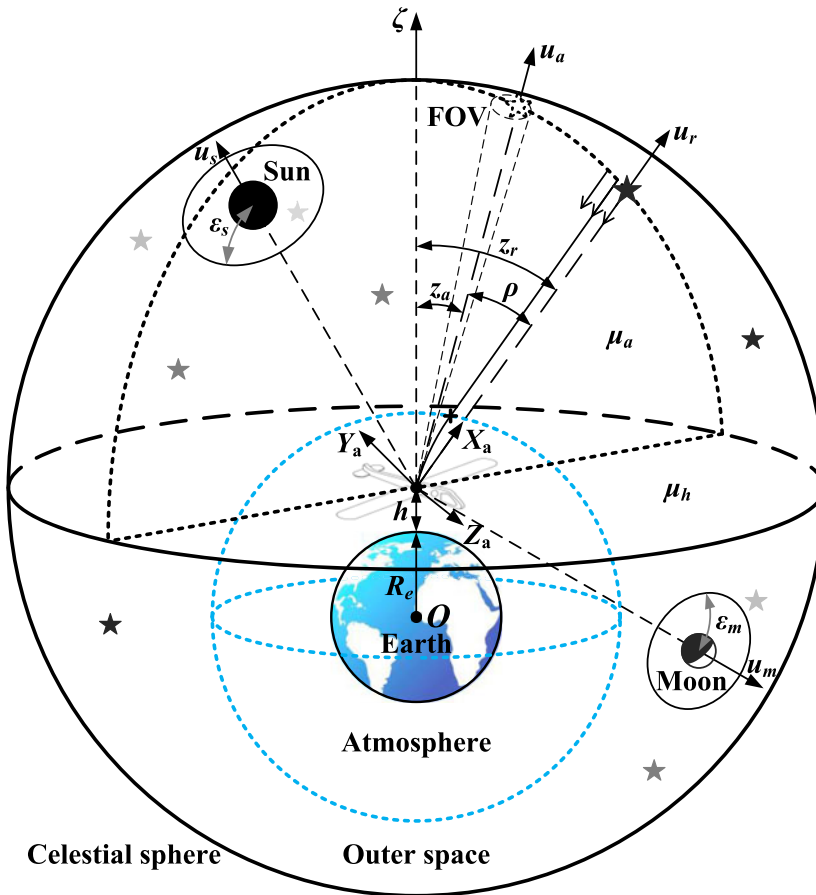


Figure 1. Geometric description of atmospheric refraction (variable scale).

where R_e is the radius of the Earth; h is the altitude of the vehicle; μ_h is the local horizon plane, $\mu_h \perp \mu_a$; \mathbf{u}_s and \mathbf{u}_m are unit directional vectors of the sun and the moon, with the exclusion angles ϵ_s and ϵ_m .

In the body coordinate system (denoted as frame b), the UAV's longitudinal axis is defined as the Y_b axis. The Z_b axis is upward in the longitudinal plane. The coordinate conversion matrix C_i^b from frame i to frame b can be calculated by the attitude determination method, with the right ascension α , declination δ and roll angle γ of the Z_b axis direction obtained from the corresponding three Euler angles: $90^\circ + \alpha$, $90^\circ - \delta$ and γ in a rotation order of 3-1-3. α , δ and γ are assigned as the absolute attitude angles of the aircraft.

The apparent stellar direction and real stellar direction in frame b are assigned as \mathbf{v}_a and \mathbf{v}_r . \mathbf{v}_a can be measured by star sensor in the star sensor coordinate system (denoted as frame s) and then transferred to frame b by the installed matrix M_b^s . When the identified star is given and the attitude is determined, \mathbf{v}_r can be obtained through \mathbf{u}_r and C_i^b . Thus,

$$\rho = \arccos(\mathbf{u}_a^T \mathbf{u}_r) = \arccos(\mathbf{v}_a^T \mathbf{v}_r) = \arccos(\mathbf{v}_a^T C_i^b \mathbf{u}_r) \tag{1}$$

In practical application, z_a can be calculated through refraction tables or empirical formulae based on the refraction angle and the ambient condition of the vehicle. In this paper, the empirical formula provided by the Chinese Astronomical Almanac (The Purple Mountain Observatory, 2021) is chosen to

analyse the problem as follows:

$$\rho_0 = \frac{\rho}{1 + \alpha_A M_A + N_A} \tag{2}$$

$$M_A = \frac{-0.00383 T_c}{1 + 0.00367 T_c} \tag{3}$$

$$N_A = \frac{P}{133.322 \times 760} - 1 \tag{4}$$

$$P = P' [1 - 0.00264 \cos 2\varphi - 0.000163(T'_c - T_c)] \tag{5}$$

$$z_a = \arctan \frac{\rho_0}{60.2''} \tag{6}$$

where ρ_0 is the mean atmospheric refractivity; M_A , N_A and α_A ($\alpha_A = 1$ generally; when z_a is large, α_A will be adjusted) are modified parameters; T_c is ambient centigrade temperature; P is ambient barometric pressure in units of Pa; T'_c is measuring centigrade temperature of mercury in the barometer; P' is measuring barometric pressure in units of Pa. Ambient barometric pressure and thermodynamic temperature T of a standard day are described by the ISA (Kurzke and Halliwell, 2018). In the range of aircraft actual flight altitude, P and T satisfy

$$P = \begin{cases} 101,325 \times \left(1 - 0.0225577 \times \frac{h}{1000}\right)^{5.25588} \text{ Pa,} & h < 11,000 \text{ m} \\ 22,632 \times e^{\frac{11000-h}{6341.62}} \text{ Pa,} & 11,000 \text{ m} \leq h \leq 25,000 \text{ m} \end{cases} \tag{7}$$

$$T = \begin{cases} 288.15 \text{ K} - 6.5 \times \frac{h}{1000}, & h < 11,000 \text{ m} \\ 216.65 \text{ K,} & 11,000 \text{ m} \leq h \leq 25,000 \text{ m} \end{cases} \tag{8}$$

Therefore,

$$z_r = z_a + \rho \tag{9}$$

The empirical formulae of Equations (2) to (9) have directly established the functional relation among z_r , z_a and ρ . For this, Ning and Wang (2013) demonstrated that the zenith error $\Delta\zeta$ increases with increasing celestial altitude (i.e., $90^\circ - z_r$) by curve-fitting method simulation. The next step is to analyse its spherical geometry.

When \mathbf{u}_r is identified, through the atmospheric refraction model, the estimated zenith direction $\hat{\zeta}$ is determined by the estimated stellar apparent direction $\hat{\mathbf{u}}_a$ with the error Δu_a which is affected by attitude accuracy, as shown in Figure 2.

The spherical triangles satisfy

$$\cos \hat{\rho} = \cos \rho \cos \Delta u_a + \sin \rho \sin \Delta u_a \cos \eta \tag{10}$$

$$\frac{\sin \beta}{\sin \Delta u_a} = \frac{\sin \eta}{\sin \hat{\rho}} \tag{11}$$

$$\cos \Delta\zeta = \cos \hat{z}_r \cos z_r + \sin \hat{z}_r \sin z_r \cos \beta \tag{12}$$

where

$$\hat{z}_r = \hat{\rho} + \arctan \frac{\hat{\rho}}{60.2''(1 + M_A + N_A)} \tag{13}$$

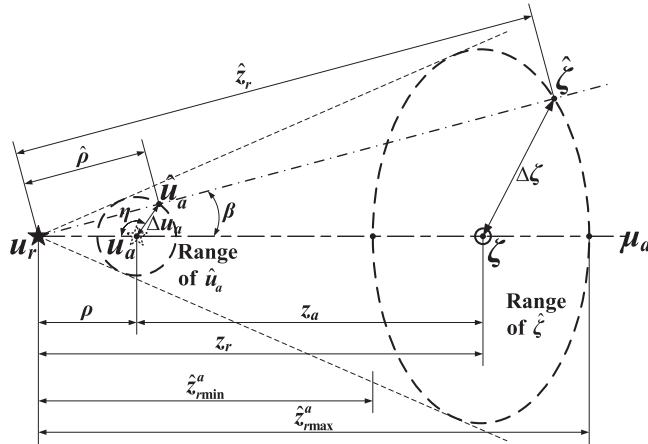


Figure 2. Geometric relationship of error ranges projected onto the celestial sphere.

Particularly in μ_a direction, the estimated real zenith distance \hat{z}_r^a satisfies

$$\begin{cases} \hat{z}_{r\min}^a = \rho - \Delta u_a + \arctan \frac{\rho - \Delta u_a}{60 \cdot 2''(1 + M_A + N_A)} & (\eta = \beta = 0) \\ \hat{z}_{r\max}^a = \rho + \Delta u_a + \arctan \frac{\rho + \Delta u_a}{60 \cdot 2''(1 + M_A + N_A)} & (\eta = 180^\circ, \beta = 0) \end{cases} \quad (14)$$

Thus

$$\Delta \hat{z}_r^a = \hat{z}_{r\max}^a - \hat{z}_{r\min}^a = 2\Delta u_a + \arctan \frac{\rho + \Delta u_a}{60 \cdot 2''(1 + M_A + N_A)} - \arctan \frac{\rho - \Delta u_a}{60 \cdot 2''(1 + M_A + N_A)} \quad (15)$$

$$\frac{d\Delta \hat{z}_r^a}{d\rho} = \frac{60 \cdot 2''(1 + M_A + N_A)}{(60 \cdot 2''(1 + M_A + N_A))^2 + (\rho + \Delta u_a)^2} - \frac{60 \cdot 2''(1 + M_A + N_A)}{(60 \cdot 2''(1 + M_A + N_A))^2 + (\rho - \Delta u_a)^2} < 0 \quad (16)$$

This indicates that the zenith error range shrinks with increasing ρ (equivalent to z_a or z_r). The whole result will be given in Section 5.1.

For the purpose of calculating the zenith direction, the stellar azimuth coordinate system (denoted as frame a) is established, with the X_a axis oriented to the stellar real direction and Y_a axis upward in plane μ_a , as shown in Figure 1. Obviously,

$$\zeta_a = [\cos z_r \quad \sin z_r \quad 0]^T \quad (17)$$

The vector-matrices V and W are established as

$$V = [V_1 \quad V_2 \quad V_3] \quad V_1 = v_r \quad V_2 = v_a \quad V_3 = \frac{v_r \times v_a}{|v_r \times v_a|} \quad (18)$$

$$W = [W_1 \quad W_2 \quad W_3] \quad W_1 = X_a = \begin{bmatrix} 1 \\ 0 \\ 0 \end{bmatrix} \quad W_2 = \begin{bmatrix} \cos \rho \\ \sin \rho \\ 0 \end{bmatrix} \quad W_3 = Z_a = \begin{bmatrix} 0 \\ 0 \\ 1 \end{bmatrix} \quad (19)$$

Hence, the orthogonalised coordinate conversion matrix C_a^b is

$$C_a^b = \frac{1}{2}(3I - C_0^T C_0) C_0^T \quad (20)$$

$$C_0 = W W^T (V V^T)^{-1} \quad (21)$$

where C_0 is the non-orthogonal matrix.

λ_b and φ_b are the longitude and latitude coordinates of zenith direction in frame b, which satisfy

$$\zeta_b = [\cos \varphi_b \cos \lambda_b \quad \cos \varphi_b \sin \lambda_b \quad \sin \varphi_b]^T = C_a^b \zeta_a \tag{22}$$

Through calculating the real-time Greenwich hour angle of Aries A_γ , the conversion matrix C_i^e from frame i to geocentric equatorial rotating coordinate system (denoted as frame e) can be obtained. Therefore, the geographical longitude λ and latitude φ can be solved by

$$[\cos \varphi \cos \lambda \quad \cos \varphi \sin \lambda \quad \sin \varphi]^T = C_i^e C_b^i \zeta_b \tag{23}$$

Assigning the east-north-zenith (E-N-U) coordinate system (denoted as frame n) as the navigation coordinate system, the conversion matrix C_n^e can be calculated through the two Euler angles $-(90^\circ - \varphi)$ and $-(90^\circ + \lambda)$ in a rotation order of 1-3. Thus the conversion matrix C_n^b can be deduced by C_i^b , C_i^e and C_n^e , with three Euler angles named respectively as yaw angle $-\psi$, pitch angle θ and roll angle ϕ in a rotation order of 3-1-2. ψ , θ and ϕ are assigned as the relative attitude angles of the aircraft.

The analysis above presents the relation between the position and attitude parameters of the UAV. However, neither the precise attitude nor position information can be directly measured by CNS alone in refractive conditions. High accuracy attitude and position determinations are key problems. In Sections 3 and 4, these will be further discussed.

3. Research on triple-FOV star sensors navigation by stellar refraction

Generally, for spacecraft, if the observed stars are successfully identified by image matching algorithm, then attitude with high accuracy can be ensured by high-precision star sensor and optimised attitude determination method. However, for aircraft, the atmosphere will absorb, scatter and refract the starlight. This may seriously decrease the light intensity and increase background noise, making starlight harder to detect, especially in daytime. As a result, both the star pattern recognition and attitude determination accuracy will be affected.

To solve these problems, the narrow FOV star sensor has been developed to improve the sensitivity of CCD (Charge Coupled Device) arrays by sacrificing the detection range. Thus, the application of multiple-FOV star sensors is necessary to ensure both the observability and the precision (Wu et al., 2015, 2019). On this basis, we can extract the refractive images from combined star map and increase the matching tolerance to maintain the recognition rate. This can be much easier or even unnecessary when sensors are working in tracking mode (Li et al., 2015; Wang et al., 2017a).

The identified stars in combined FOV are shown in Figure 3, where S_j ($j = 1, 2, 3$) are boresight projections on the celestial sphere corresponding to star sensor I, II or III. For each observed star, the projections of u_{al} , u_{rl} and ζ are on the arc where the celestial sphere meets with μ_{al} ($l = 1, 2, 3, \dots$).

Obviously, ζ is the common intersecting line of all the stellar azimuth planes. When the precise ζ is calculated, the position can be acquired. However, according to Section 2, calculations of the zenith direction and attitude are coupled. So the following two schemes are designed to seek the efficient method.

3.1. Coplanar distribution scheme

When a UAV is cruising straight and level, the Z_b axis can be considered as orienting to the zenith. That means that, if the observed starlight orientation is close to the Z_b axis (Star 1 and 2 in Sensor I), then ρ will be very small, i.e.,

$$\begin{cases} u_{al} \approx u_{rl} \\ v_{al} \approx v_{rl} \end{cases} \quad (l = 1, 2) \tag{24}$$

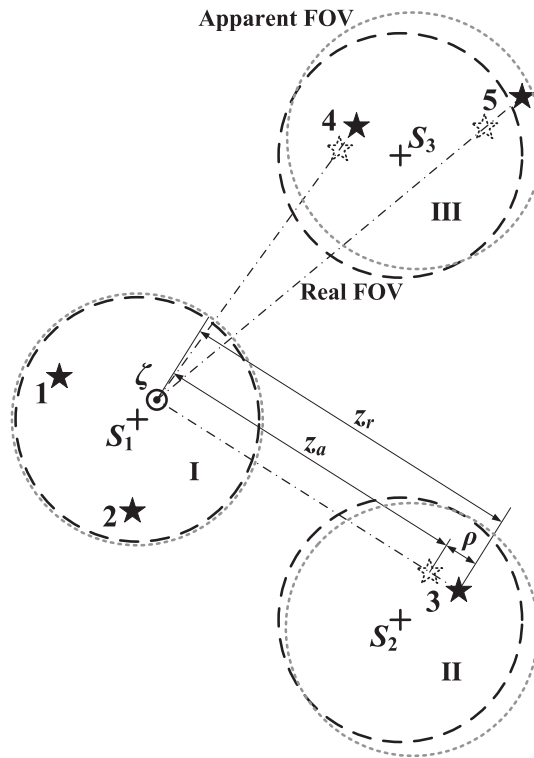


Figure 3. Geometric relationship of multiple FOVs and stars projected onto the celestial sphere.

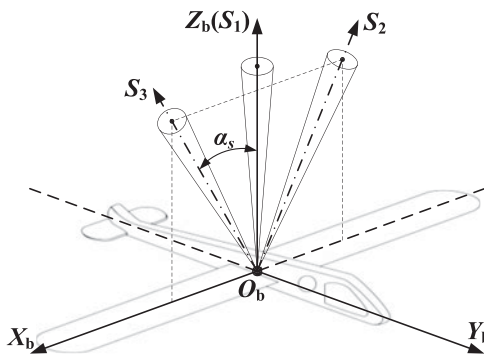


Figure 4. Installation of the coplanar distribution scheme.

Therefore the absolute attitude of the vehicle can be directly determined by at least two identified stars in theory (Shuster and Oh, 1981; Zhu et al., 2017). Based on this, a coplanar distribution scheme by three star sensors is designed to analyse the problem, as shown in Figure 4, where α_s ($0 \leq \alpha_s \leq 90^\circ$) is marked as the strapdown installation angle.

Sensor I is used to measure the ‘non-refracted’ stars and estimate the attitude, whereas Sensors II and III, in a symmetrical distribution, are utilised to observe the refracted stars and calculate the geographical coordinates by the atmospheric refraction model with \hat{C}_i^b provided by Sensor I. Furthermore,

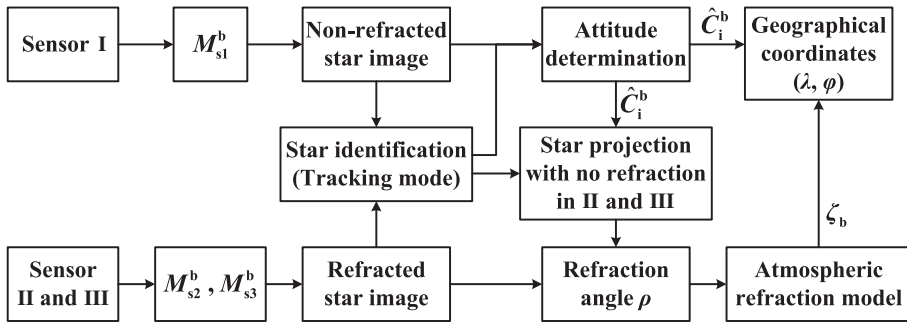


Figure 5. Flowchart of the coplanar distribution scheme.

sensors on both sides can increase the observation scope and ensure the FOVs do not scan blind areas (e.g. the sun and the moon) simultaneously. The flowchart is presented in Figure 5.

However, this scheme has two disadvantages. First, limited by the FOV of Sensor I, the detection probability is low and the angular distance between different starlight vectors is rather small, which may lead to big errors in attitude. Second, when the aircraft manoeuvres in flight, boresight of Sensor I will deviate from the zenith direction and refraction cannot be ignored. Therefore, general cases should be studied.

3.2. Triangular distribution scheme

The universality of triple-FOV star sensors in triangular distribution can enhance the practicability of CNS. These are installed, as shown in Figure 6, to satisfy the omnibearing observation.

Through derivation of the Jacobi identity (see Appendix part in details),

$$(\mathbf{v}_a \times \mathbf{v}_r \cdot \zeta_b)^2 = 1 - (\mathbf{v}_a \cdot \mathbf{v}_r)^2 - (\mathbf{v}_r \cdot \zeta_b)^2 - (\zeta_b \cdot \mathbf{v}_a)^2 + 2(\mathbf{v}_a \cdot \mathbf{v}_r)(\mathbf{v}_r \cdot \zeta_b)(\zeta_b \cdot \mathbf{v}_a) = 0 \quad (25)$$

Based on this, the loss function (Wang et al., 2021a) is established as

$$\begin{aligned}
 F(\mathbf{C}_i^b, \zeta_b) &= \sum_{l=1}^n a_l (\mathbf{v}_{al} \times \mathbf{v}_{rl} \cdot \zeta_b)^2 \\
 &= \sum_{l=1}^n a_l (1 - (\mathbf{v}_{al}^T \mathbf{C}_i^b \mathbf{u}_{rl})^2 - (\zeta_b^T \mathbf{C}_i^b \mathbf{u}_{rl})^2 - (\zeta_b^T \mathbf{v}_{al})^2 + 2(\mathbf{v}_{al}^T \mathbf{C}_i^b \mathbf{u}_{rl})(\zeta_b^T \mathbf{C}_i^b \mathbf{u}_{rl})(\zeta_b^T \mathbf{v}_{al})) \quad (26)
 \end{aligned}$$

where n is the total number of observed stars, $a_l (l = 1, \dots, n)$ are a set of nonnegative weights satisfying

$$\sum_{l=1}^n a_l = 1 \quad (27)$$

Obviously, the less estimated errors of $\hat{\mathbf{C}}_i^b$ and $\hat{\zeta}_b$ are, the smaller function value is. Combined with Equation (22), variables of the loss function are converted into two scalars (λ_b and φ_b) and one matrix, which cannot be solved by existing classical methods on account of strong nonlinearity. Now we try to establish a conjugate gradient iterative algorithm to testify the improvement of navigation accuracy by reducing the loss function value.

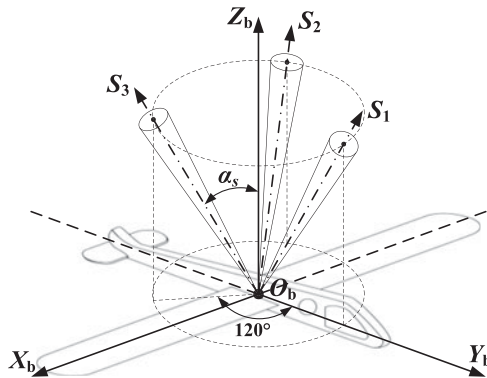


Figure 6. Installation of the triangular distribution scheme.

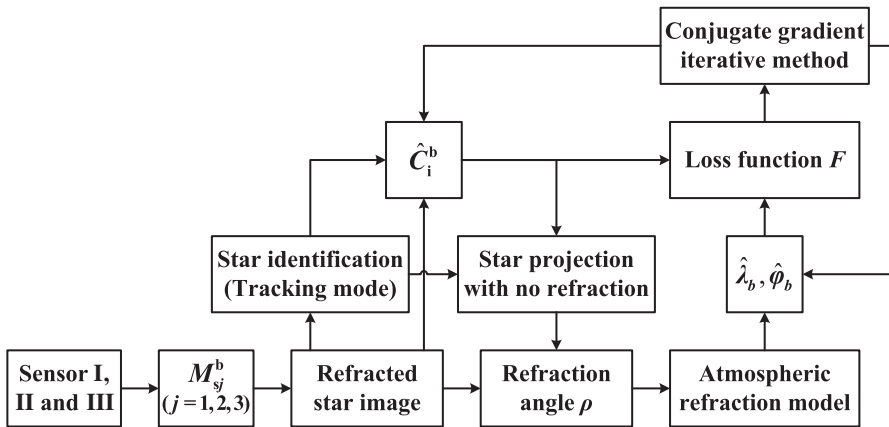


Figure 7. Flowchart of the triangular distribution scheme.

Actual observed stars are measured in the combined FOV of I, II and III, so a rough attitude \hat{C}_i^b can be estimated without refraction compensation, thereby obtaining $\hat{\lambda}_b$ and $\hat{\varphi}_b$ in a similar way. Regarding \hat{C}_i^b as a constant matrix in each iteration, the loss function can be processed by conjugate gradient iterative method to update attitude and position information, as shown in Rivaie et al., 2015; Liu et al., 2018).

The gradient function satisfies

$$\mathbf{g} = \left[\frac{\partial F}{\partial \lambda_b} \quad \frac{\partial F}{\partial \varphi_b} \right]^T \tag{28}$$

$$\frac{\partial F}{\partial \lambda_b} = \frac{\partial \zeta_b^T}{\partial \lambda_b} \cdot \frac{\partial F}{\partial \zeta_b} = [-\cos \hat{\varphi}_b \sin \hat{\lambda}_b \quad \cos \hat{\varphi}_b \cos \hat{\lambda}_b \quad 0] \cdot \frac{\partial F}{\partial \zeta_b} \tag{29}$$

$$\frac{\partial F}{\partial \varphi_b} = \frac{\partial \zeta_b^T}{\partial \varphi_b} \cdot \frac{\partial F}{\partial \zeta_b} = [-\sin \hat{\varphi}_b \cos \hat{\lambda}_b \quad -\sin \hat{\varphi}_b \sin \hat{\lambda}_b \quad \cos \hat{\varphi}_b]^T \cdot \frac{\partial F}{\partial \zeta_b} \tag{30}$$

$$\frac{\partial F}{\partial \zeta_b} = (-2) \cdot \left[\sum_{l=1}^n a_l v_{al} v_{al}^T + \hat{C}_i^b \left(\sum_{l=1}^n a_l \mathbf{u}_{rl} \mathbf{u}_{rl}^T \right) \hat{C}_i^b - \sum_{l=1}^n a_l v_{al}^T \hat{C}_i^b \mathbf{u}_{rl} (v_{al} (\hat{C}_i^b \mathbf{u}_{rl})^T + \hat{C}_i^b \mathbf{u}_{rl} v_{al}^T) \right] \cdot \hat{\zeta}_b \tag{31}$$

Therefore, the conjugate gradient iterative method contains the following steps:

Step 1: When $\|\mathbf{g}_k\| \leq \epsilon$ ($k=0, 1, 2, \dots, \epsilon$ is the specified precision), iteration algorithm stops.

Step 2: Determine the iteration step length α_k by Armijo line search method (Nocedal and Wright, 2006). Then,

$$\begin{bmatrix} \hat{\lambda}_b \\ \hat{\varphi}_b \end{bmatrix}_{k+1} = \begin{bmatrix} \hat{\lambda}_b \\ \hat{\varphi}_b \end{bmatrix}_k + \alpha_k \mathbf{d}_k \tag{32}$$

where the initial search direction $\mathbf{d}_0 = -\mathbf{g}_0$.

Step 3: Revise the refracted starlight by $(\hat{\lambda}_b, \hat{\varphi}_b)_{k+1}$ through atmospheric refraction model and update the attitude $\hat{\mathbf{C}}_i^b$.

Step 4: Compute F_{k+1} and \mathbf{g}_{k+1} by $\hat{\mathbf{C}}_i^b$ and $(\hat{\lambda}_b, \hat{\varphi}_b)_{k+1}$.

Step 5: Compute β_{k+1} by

$$\beta_{k+1} = \frac{\mathbf{g}_{k+1}^T (\mathbf{g}_{k+1} - \mathbf{g}_k - \mathbf{d}_k)}{\|\mathbf{d}_k\|^2} \tag{33}$$

Step 6: Compute \mathbf{d}_{k+1} by

$$\mathbf{d}_{k+1} = -\mathbf{g}_{k+1} + \beta_{k+1} \mathbf{d}_k - \frac{\mathbf{g}_{k+1}^T \mathbf{d}_k}{\|\mathbf{d}_k\|^2} F_k \tag{34}$$

Step 7: Set $k := k + 1$, go to step 1.

The authors expected to obtain an accurate result by the gradient iterative algorithm above. However, the iteration cannot efficiently converge to the given nominal condition, when ignoring the influence of attitude on gradient. Its uncertainty will be demonstrated in Section 5.2.

Indeed, the common principle of the double schemes above is to correct the position through a rough attitude provided by CNS. It can be easily verified that the tiny attitude error will be amplified by the atmospheric refraction model and then seriously affect the position accuracy. If an initial location can be given, through the reverse process, a precise attitude will be acquired. Maybe SINS can do this.

4. SIMU/triple star sensors deep integrated method in refractive effect

The traditional INS/CNS deep integrated method without refraction correction can be designed as in Figure 8. In the INS section, specific forces f_E, f_N, f_U along the three axes can be calculated through ω_{ib}^b provided by gyroscope and α_{ib}^b provided by accelerometer. On the basis of dynamic relationship, position parameters $\hat{\varphi}, \hat{\lambda}, \hat{h}$ and attitude parameters $\hat{\theta}, \hat{\phi}, \hat{\psi}$ can be acquired, thus obtaining $\hat{\zeta}_b$ (fused with initial location and horizontal reference) and matrix of misalignment angle \mathbf{M}_S . Owing to the non-damping and instability in altitude channel of INS (Qin, 2006), as well as the non-observability of altitude in CNS, the nominal altitude h_r will be directly given by altimeter in this paper.

In the CNS section, to ensure high-precision navigation in long-endurance flight, three (or two at least) FOVs should be available to detect stars, whose numbers of observed stars are N_1, N_2 and N_3 . Thus, the identified $\mathbf{u}_{r,l}$ and the measured $\mathbf{v}_{a,l}$ can determine $\hat{\mathbf{C}}_i^b$ then calculate position parameters φ, λ and attitude parameters θ, ϕ, ψ through $\hat{\zeta}_b$ provided by INS.

Now, the new deep integrated method with refraction correction is shown as Figure 9.

Based on the atmospheric refraction model, $\hat{\mathbf{C}}_i^b$ determined by the identified $\mathbf{u}_{r,l}$ and the corrected $\hat{\mathbf{v}}_{r,l}$ is more precise. The updated $\mathbf{v}_{r,l}$ (calculated by $\hat{\mathbf{C}}_i^b$ and $\mathbf{u}_{r,l}$) and the measured $\mathbf{v}_{a,l}$ can then determine the corrected $\zeta_{b,l}$ of each observed star. Calculate $\bar{\zeta}_b$ as

$$\bar{\zeta}_b = \frac{\sum_{l=1}^{N_1+N_2+N_3} \zeta_{bl}}{\left\| \sum_{l=1}^{N_1+N_2+N_3} \zeta_{bl} \right\|} \tag{35}$$

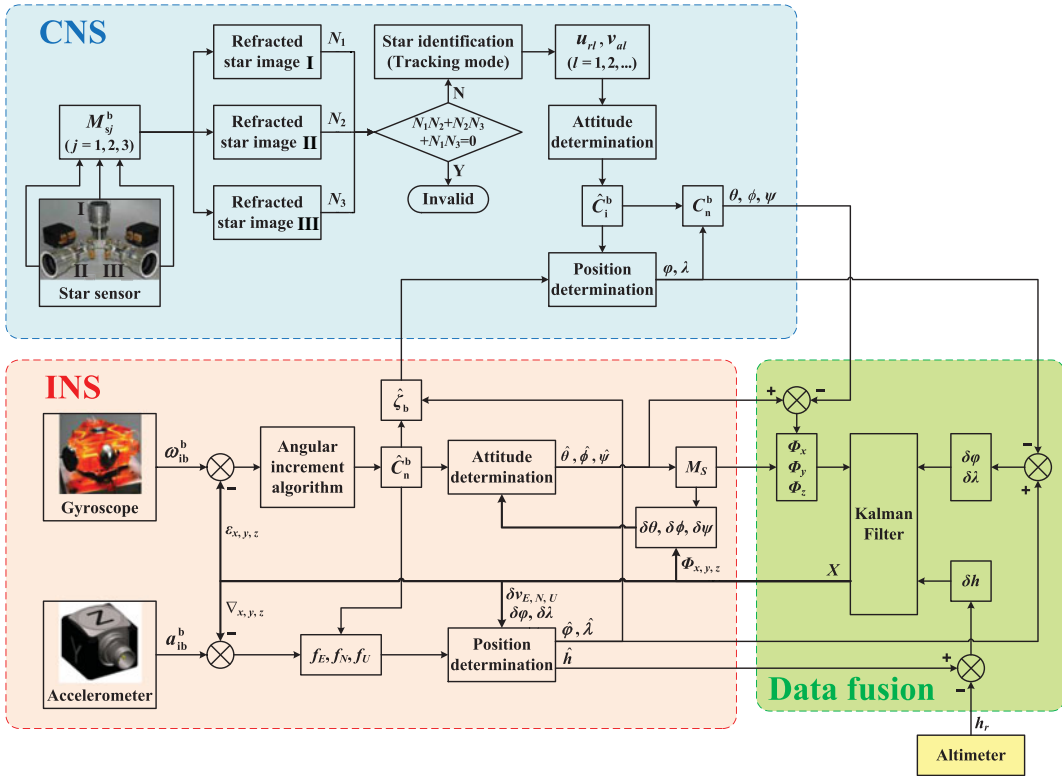


Figure 8. Flowchart of SIMU/triple star sensors deep integrated without refraction correction.

thus obtaining $\bar{\varphi}, \bar{\lambda}$ (i.e., φ, λ) followed with θ, ϕ, ψ .

Kalman filter is utilised to realise the data fusion (Pan et al., 2013). The navigation deviations are denoted as

$$\begin{cases} \delta\theta = \hat{\theta} - \theta \\ \delta\phi = \hat{\phi} - \phi \\ \delta\psi = \hat{\psi} - \psi \\ \delta\varphi = \hat{\varphi} - \varphi \\ \delta\lambda = \hat{\lambda} - \lambda \\ \delta h = \hat{h} - h_r \end{cases} \quad (36)$$

So the misalignment angles Φ_x, Φ_y, Φ_z can be determined by (Zhu et al., 2018)

$$\begin{bmatrix} \Phi_x \\ \Phi_y \\ \Phi_z \end{bmatrix} = M_S \begin{bmatrix} \delta\theta \\ \delta\phi \\ \delta\psi \end{bmatrix} = \begin{bmatrix} -\cos \hat{\psi} & -\sin \hat{\psi} \cos \hat{\theta} & 0 \\ \sin \hat{\psi} & -\cos \hat{\psi} \cos \hat{\theta} & 0 \\ 0 & -\sin \hat{\theta} & 1 \end{bmatrix} \begin{bmatrix} \delta\theta \\ \delta\phi \\ \delta\psi \end{bmatrix} \quad (37)$$

According to the error equations of SINS, build the 15-dimensional state model as follows

$$X = [\delta v_E \ \delta v_N \ \delta v_U \ \Phi_x \ \Phi_y \ \Phi_z \ \delta\varphi \ \delta\lambda \ \delta h \ \varepsilon_x \ \varepsilon_y \ \varepsilon_z \ \nabla_x \ \nabla_y \ \nabla_z]^T \quad (38)$$

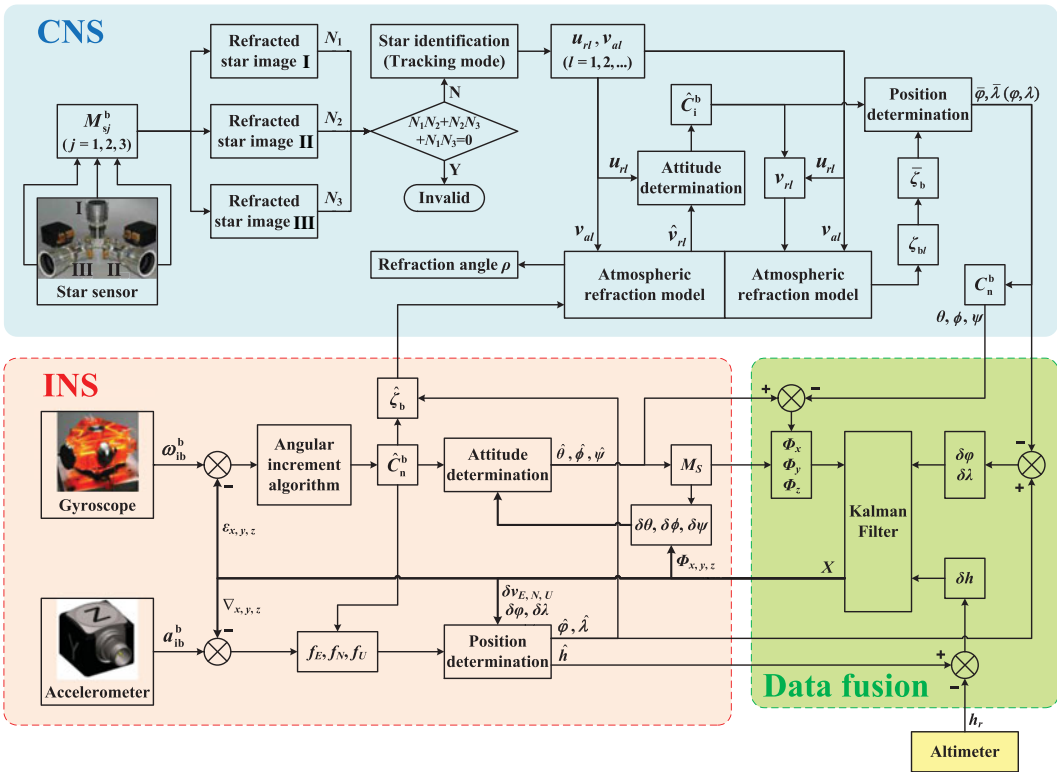


Figure 9. Flowchart of SIMU/triple star sensors deep integrated with refraction correction.

where $\delta v_E, \delta v_N, \delta v_U$ are velocity deviations; $\epsilon_x, \epsilon_y, \epsilon_z$ are gyroscope drifts; $\nabla_x, \nabla_y, \nabla_z$ are accelerometer biases. The state equation is

$$\dot{X} = FX + GW_{SINS} \tag{39}$$

$$F = \begin{bmatrix} F_N(9 \times 9) & F_S(6 \times 6) \\ \mathbf{0}_{6 \times 9} & \mathbf{0}_{9 \times 6} \end{bmatrix} \tag{40}$$

$$G = \begin{bmatrix} \mathbf{0}_{3 \times 3} & C_b^n \\ -C_b^n & \mathbf{0}_{3 \times 3} \\ \mathbf{0}_{9 \times 3} & \mathbf{0}_{9 \times 3} \end{bmatrix} \tag{41}$$

$$W_{SINS} = [\omega_{\epsilon x} \ \omega_{\epsilon y} \ \omega_{\epsilon z} \ \omega_{\nabla x} \ \omega_{\nabla y} \ \omega_{\nabla z}]^T \tag{42}$$

where $\omega_{\epsilon x}, \omega_{\epsilon y}, \omega_{\epsilon z}$ are gyroscope noises; $\omega_{\nabla x}, \omega_{\nabla y}, \omega_{\nabla z}$ are accelerometer noises. Non-zero elements of F_N are (Qin, 2006; Li et al., 2018)

$$F_N(1, 1) = \frac{v_N \tan \hat{\varphi} - v_U}{R_N + \hat{h}}, F_N(1, 2) = 2\omega_{ie} \sin \hat{\varphi} + \frac{v_E \tan \hat{\varphi}}{R_N + \hat{h}},$$

$$F_N(1, 3) = -\left(2\omega_{ie} \cos \hat{\varphi} + \frac{v_E}{R_N + \hat{h}}\right), F_N(1, 5) = -f_U, F_N(1, 6) = f_N,$$

$$F_N(1, 7) = 2\omega_{ie}(v_U \sin \hat{\varphi} + v_N \cos \hat{\varphi}) + \frac{v_E v_N \sec^2 \hat{\varphi}}{R_N + \hat{h}}, F_N(1, 9) = \frac{v_E v_U - v_E v_N \tan \hat{\varphi}}{(R_N + \hat{h})^2},$$

$$F_N(2, 1) = -F_N(1, 2), F_N(2, 2) = -\frac{v_U}{R_M + \hat{h}}, F_N(2, 3) = -\frac{v_N}{R_M + \hat{h}}, F_N(2, 4) = f_U,$$

$$\begin{aligned}
 F_N(2, 6) &= -f_E, F_N(2, 7) = -\left(2\omega_{ie}v_E \cos \hat{\varphi} + \frac{v_E^2 \sec^2 \hat{\varphi}}{R_N + \hat{h}}\right), \\
 F_N(2, 9) &= \frac{v_N v_U}{(R_M + \hat{h})^2} + \frac{v_E^2 \tan \hat{\varphi}}{(R_N + \hat{h})^2}, F_N(3, 1) = 2\omega_{ie} \cos \hat{\varphi} + \frac{2v_E}{R_N + \hat{h}}, F_N(3, 2) = \frac{2v_N}{R_M + \hat{h}}, \\
 F_N(3, 4) &= -f_N, F_N(3, 5) = f_E, F_N(3, 7) = -2\omega_{ie}v_E \sin \hat{\varphi}, \\
 F_N(3, 9) &= -\frac{v_N^2}{(R_M + \hat{h})^2} - \frac{v_E^2}{(R_N + \hat{h})^2}, F_N(4, 2) = -\frac{1}{R_M + \hat{h}}, F_N(4, 5) = \omega_{ie} \sin \hat{\varphi} + \frac{v_E \tan \hat{\varphi}}{R_N + \hat{h}}, \\
 F_N(4, 6) &= -\omega_{ie} \cos \hat{\varphi} - \frac{v_E}{R_N + \hat{h}}, F_N(4, 9) = \frac{v_N}{(R_M + \hat{h})^2}, F_N(5, 1) = \frac{1}{R_N + \hat{h}}, \\
 F_N(5, 4) &= -F_N(4, 5), F_N(5, 6) = F_N(2, 3), F_N(5, 7) = -\omega_{ie} \sin \hat{\varphi}, \\
 F_N(5, 9) &= -\frac{v_E}{(R_N + \hat{h})^2}, F_N(6, 1) = \frac{\tan \hat{\varphi}}{R_N + \hat{h}}, F_N(6, 4) = -F_N(4, 6), F_N(6, 5) = -F_N(2, 3), \\
 F_N(6, 7) &= \omega_{ie} \cos \hat{\varphi} + \frac{v_E \sec^2 \hat{\varphi}}{R_N + \hat{h}}, F_N(6, 9) = -\frac{v_E \tan \hat{\varphi}}{(R_N + \hat{h})^2}, F_N(7, 2) = -F_N(4, 2), \\
 F_N(7, 9) &= -F_N(4, 9), F_N(8, 1) = \frac{\sec \hat{\varphi}}{R_N + \hat{h}}, F_N(8, 7) = v_E \tan \hat{\varphi} F_N(8, 1), \\
 F_N(8, 9) &= F_N(5, 9) \sec \hat{\varphi}, F_N(9, 3) = 1,
 \end{aligned}$$

where R_M is the main radius of curvature of the meridian; R_N is the main radius of curvature of prime vertical; ω_{ie} is the rotational angular velocity of the Earth.

$$F_S = \begin{bmatrix} \mathbf{0}_{3 \times 3} & \mathbf{C}_b^n \\ -\mathbf{C}_b^n & \mathbf{0}_{3 \times 3} \end{bmatrix} \tag{43}$$

Build the six-dimensional measurement model as follows

$$\mathbf{Z} = [\Phi_x \ \Phi_y \ \Phi_z \ \delta\varphi \ \delta\lambda \ \delta h]^T \tag{44}$$

The measurement equation is

$$\mathbf{Z} = \mathbf{H}\mathbf{X} + \mathbf{V}_m \tag{45}$$

$$\mathbf{H} = [\mathbf{0}_{6 \times 3} \ \mathbf{I}_{6 \times 6} \ \mathbf{0}_{6 \times 6}] \tag{46}$$

where \mathbf{V}_m is measuring noise.

Generally, the data output rate of the SIMU is higher than the star sensor. During the interval of CNS output, INS alone calculates and updates the navigation parameters and matrix \mathbf{P} in Kalman filter. Otherwise, data fusion proceeds and the final filtering result \mathbf{X} will be feedback to INS and compensate for the state errors. Then \mathbf{X} will be reset to zero until the next filtering moment.

5. Simulation verification and analysis

In this section, simulation of the zenith error range located by different zenith distances will be given first. Then, both the static simulations of CNS with the coplanar distribution scheme (assigned as Scheme 1) and the triangular distribution scheme (assigned as Scheme 2), as well as the dynamic simulations of SINS/CNS deep integrated with Scheme 2, will be discussed.

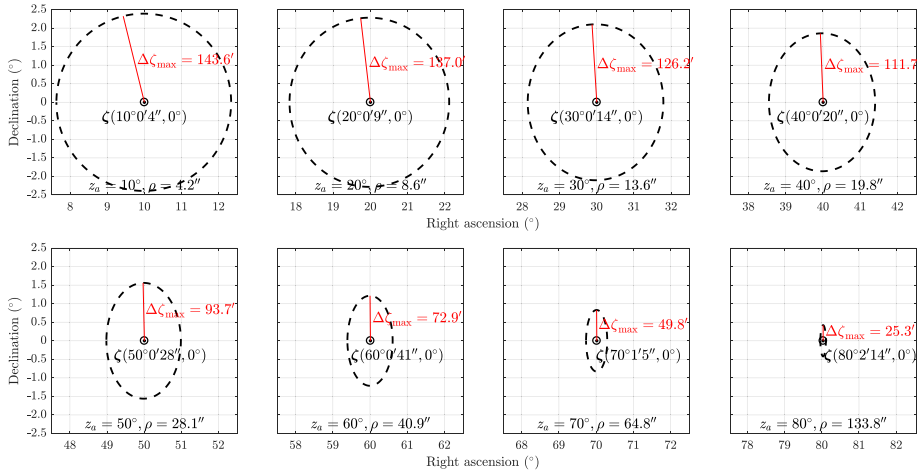


Figure 10. Zenith error ranges with different zenith distances.

5.1. Simulation of the zenith error range

According to Figure 2, assign μ_a as the celestial equator, u_r orienting to the vernal equinox, $(\hat{\alpha}_\zeta, \hat{\delta}_\zeta)$ as the right ascension and declination of $\hat{\zeta}$, then $\zeta(z_r, 0)$. Obviously,

$$\begin{cases} [\cos \hat{\delta}_\zeta \cos \hat{\alpha}_\zeta \cos \hat{\delta}_\zeta \sin \hat{\alpha}_\zeta \sin \hat{\delta}_\zeta] \cdot [1 \ 0 \ 0]^T = \cos \hat{z}_r \\ [\cos \hat{\delta}_\zeta \cos \hat{\alpha}_\zeta \cos \hat{\delta}_\zeta \sin \hat{\alpha}_\zeta \sin \hat{\delta}_\zeta] \cdot [\cos z_r \ \sin z_r \ 0]^T = \cos \Delta\zeta \\ \text{sgn}(\hat{\delta}_\zeta) = \text{sgn}(\beta) \end{cases}$$

Therefore, combined with Equation (12),

$$\begin{cases} \hat{\alpha}_\zeta = \arctan(\tan \hat{z}_r \cos \beta) \\ \hat{\delta}_\zeta = \text{sgn}(\beta) \arccos \sqrt{\sin^2 \hat{z}_r \cos^2 \beta + \cos^2 \hat{z}_r} \end{cases}$$

Setting $\Delta u_a = 1''$, $h = 15$ km, then the zenith error ranges in various conditions are shown in Figure 10.

It can be seen that both the error range and $\Delta\zeta_{\max}$ decrease with increasing zenith distance. However, even if $\Delta\zeta$ is about $25'$ (e.g. $z_a = 80^\circ$, $\Delta\zeta_{\max} = 25.3'$), the position error will be up to 46 km (one arc minute gives an error in coordinates of approximately one nautical mile, i.e., 1.852 km) on the Earth's surface, let alone the larger Δu_a in actual flight.

It should be noted that refraction effects in the vicinity of the horizon are more complicated (Yu et al., 2015). Therefore, the optimal navigation star for positioning should be located high enough above the horizon.

5.2. Static simulation of CNS

In static simulations without any measurement noise, the Monte Carlo method with 200 times independent repeated experiments will be used to calculate the root mean square error (RMSE) of navigation parameters. Setting $h = 15$ km, $\alpha_s = 70^\circ$, corresponding $\alpha_A = 1.009$ (The Purple Mountain Observatory, 2021), $C_i^e = I_{3 \times 3}$.

5.2.1. Precision analysis with Scheme 1

On the condition that the Z_b axis orients to the zenith, λ , φ and ψ are randomly generated. According to Fan and Li's study (2011), the initial limiting magnitude (denoted as M) of star sensors I, II and III was

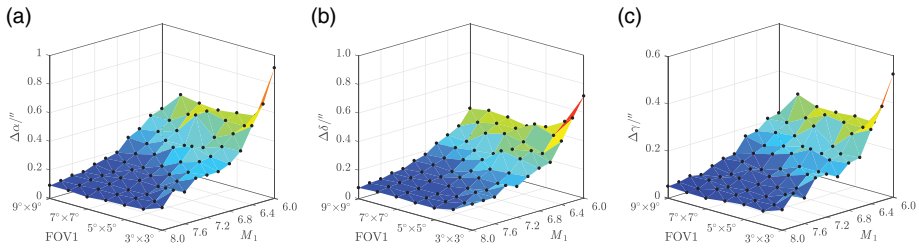


Figure 11. Absolute attitude RMSE: (a) right ascension error (b) declination error (c) roll error.

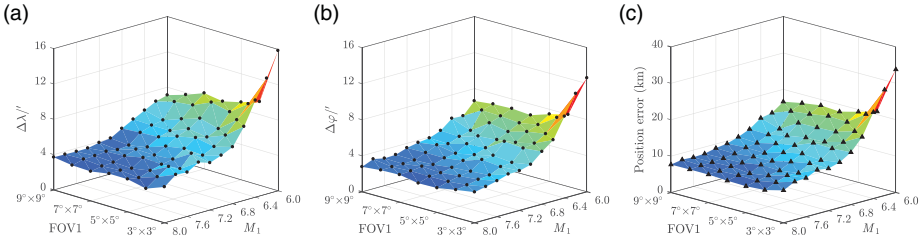


Figure 12. Position RMSE: (a) longitude error (b) latitude error (c) total position error.

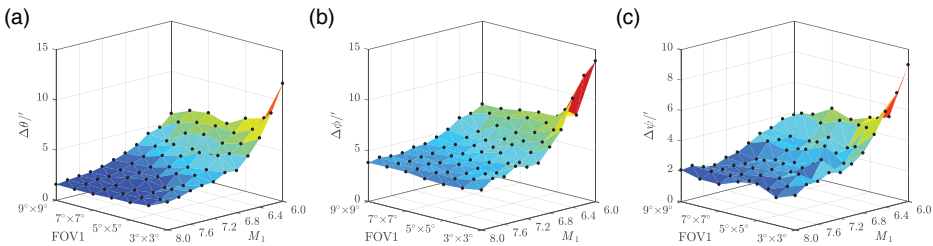


Figure 13. Relative attitude RMSE: (a) pitch error (b) roll error (c) yaw error.

set as 8.0, with FOV $3^\circ \times 3^\circ$. Then, the FOV of Sensor I was changed from $3^\circ \times 3^\circ$ to $9^\circ \times 9^\circ$, and M_1 from 8.0 to 6.0. Sensors II and III remain unchanged. The simulation results are shown in Figures 11–13.

Obviously, with the decrease of M_1 and FOV1, which indicate fewer stars being detected, both the attitude error and position error tend to increase. Besides, as shown in Figure 10, $\rho < 4.2''$ when $z_a < 10^\circ$, $h = 15$ km. Although the absolute attitude RMSE is strictly limited within $1''$, the position RMSE and relative attitude RMSE, however, are still big enough especially for positioning, let alone with manoeuvre or measurement noise in calculation. This indicates that Scheme 1 has low engineering feasibility.

5.2.2. Precision and loss function analyses with Scheme 2

Sensors I, II and III with FOV $3^\circ \times 3^\circ$ are equivalent. M_j ($j = 1, 2, 3$) is reduced from 8.0 to 6.0. The observation results are shown in Figure 14 where the success ratio of attitude determination is the percentage that at least two stars can be observed in 200 samples. It can be seen that both the number of observed stars and the success ratio decrease with reducing M . Ensuring the detectivity of each star sensor is vitally important in actual flight. Therefore, $M_j \geq 6.4$, $\bar{N}_j > 1$ ($j = 1, 2, 3$) with success ratio higher than 90% should be satisfied in practice to ensure real-time accuracy, as set out in Section 5.3.

For each sample where attitude was successfully determined, the attitude determination method without refraction corrected is assigned as Case 1, the method with only two FOVs available with refraction corrected is assigned as Case 2 and the method with all three FOVs available with refraction corrected as Case 3. Thereinto, the nominal location is given in Case 2 and Case 3. The simulation results of the absolute attitude error are shown in Figure 15 and Table 1.

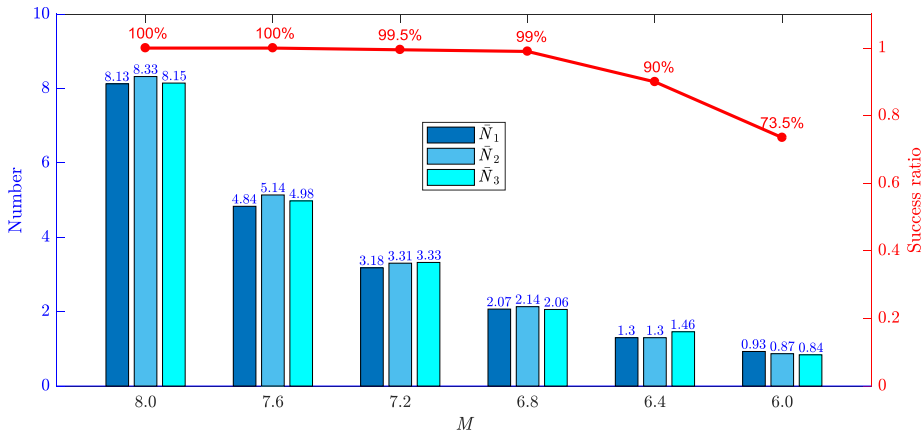


Figure 14. Mean number of observed stars and success ratio of attitude determination.

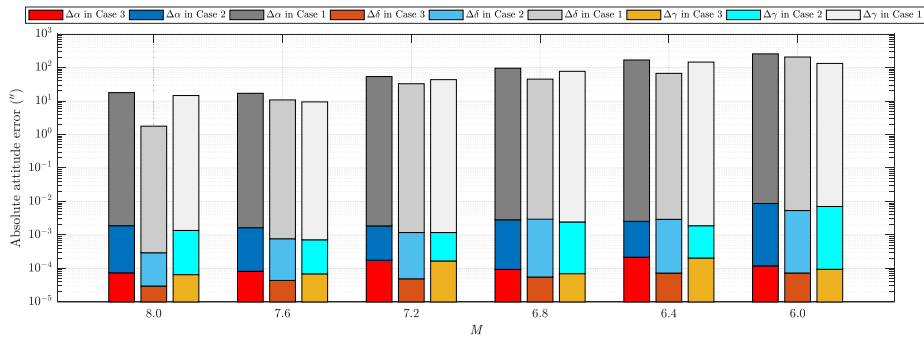


Figure 15. Attitude RMSE in the three cases.

Table 1. Attitude RMSE in the three cases.

	M	8·0	7·6	7·2	6·8	6·4	6·0
Case 1	$\Delta\alpha''$	17·77	17·04	53·84	95·53	168·22	256·41
	$\Delta\delta''$	1·77	10·80	32·83	45·06	67·00	206·35
	$\Delta\gamma''$	14·59	9·43	43·49	77·12	145·46	132·83
Case 2	$\Delta\alpha''$	$1·89 \times 10^{-3}$	$1·65 \times 10^{-3}$	$1·87 \times 10^{-3}$	$2·84 \times 10^{-3}$	$2·55 \times 10^{-3}$	$8·71 \times 10^{-3}$
	$\Delta\delta''$	$2·95 \times 10^{-4}$	$7·72 \times 10^{-4}$	$1·18 \times 10^{-3}$	$2·96 \times 10^{-3}$	$2·93 \times 10^{-3}$	$5·37 \times 10^{-3}$
	$\Delta\gamma''$	$1·37 \times 10^{-3}$	$7·19 \times 10^{-4}$	$1·18 \times 10^{-3}$	$2·45 \times 10^{-3}$	$1·89 \times 10^{-3}$	$7·10 \times 10^{-3}$
	$\Delta\alpha'''$	$7·42 \times 10^{-5}$	$8·26 \times 10^{-5}$	$1·77 \times 10^{-4}$	$9·39 \times 10^{-5}$	$2·17 \times 10^{-4}$	$1·20 \times 10^{-4}$
Case 3	$\Delta\delta''$	$2·99 \times 10^{-5}$	$4·39 \times 10^{-5}$	$4·91 \times 10^{-5}$	$5·55 \times 10^{-5}$	$7·28 \times 10^{-5}$	$7·32 \times 10^{-5}$
	$\Delta\gamma''$	$6·55 \times 10^{-5}$	$6·91 \times 10^{-5}$	$1·68 \times 10^{-4}$	$7·00 \times 10^{-5}$	$2·05 \times 10^{-4}$	$9·45 \times 10^{-5}$

Obviously, the attitude precision determined by Case 1 is rough. Case 2 is worse than Case 3, despite its computational attitude RMSE with finite bit capacity of the processor in algorithm simulation having already been equal to zero under the ideal conditions. In the long-endurance flight condition, Case 2 can be considered as an alternative.

The next step is to verify the feasibility of the conjugate gradient iterative method mentioned in Section 3.2. Set $M = 8·0$. Assign $\lambda_{b0} = 151·22^\circ$ and $\varphi_{b0} = 85·39^\circ$, solved by a random flight status as the nominal location. Then, separately plot the loss function in the domain around $(\lambda_{b0}, \varphi_{b0})$ with attitudes

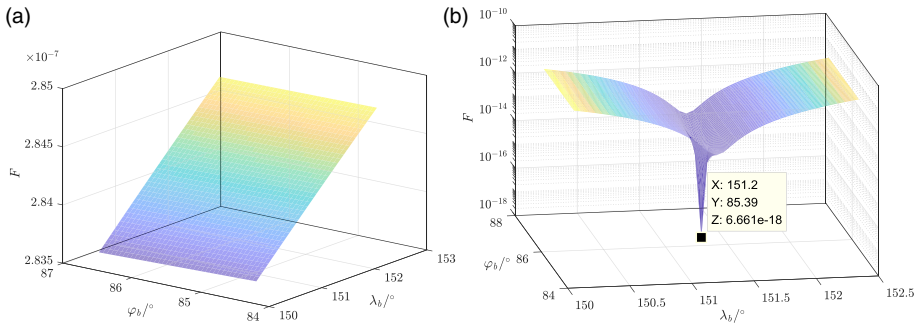


Figure 16. Loss function simulation: (a) attitude determined by Case 1, (b) attitude determined by Case 3.

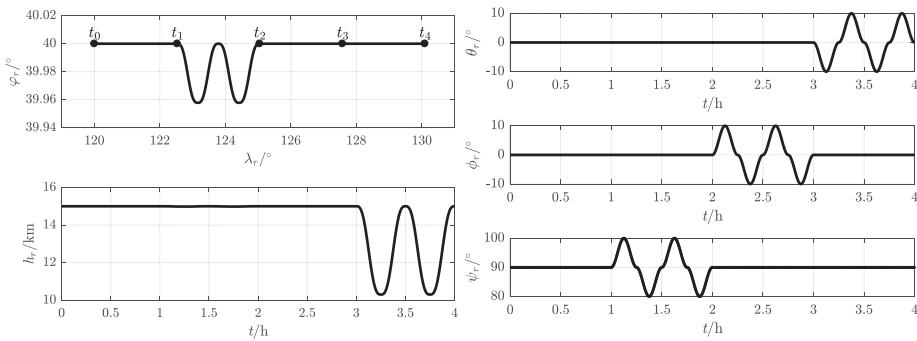


Figure 17. Real kinematic parameters of UAV.

determined by Case 1 and Case 3, as in Figure 16, where $a_l = 1/(N_1 + N_2 + N_3)$ ($l = 1, \dots, N_1 + N_2 + N_3$). It can be seen that the loss function is non-convex when the rough attitude (Case 1) is given. Only if the precise attitude (Case 3) is acquired can $(\hat{\lambda}_b, \hat{\varphi}_b)$ converge to $(\lambda_{b0}, \varphi_{b0})$ with loss function minimised. However, this is difficult to realise in application with refraction influence.

5.3. Dynamic simulation of SINS/CNS

5.3.1. Environment settings

A simplified nominal flight trajectory with manoeuvring in the stratosphere is designed to verify the integrated method. One flight cycle is set at 4 h with time nodes t_0, t_1, t_2, t_3, t_4 at intervals of 1 h. The UAV’s velocity is set at 60 m/s constantly orienting to the Y_b axis (attack angle is 0° , sideslip angle is 0°) and the initial real (nominal) kinematic parameters satisfy $(\varphi_r(t_0), \lambda_r(t_0)) = (40^\circ, 120^\circ)$, $h_r(t_0) = 15$ km, $\theta_r(t_0) = \varphi_r(t_0) = 0^\circ$, $\psi_r(t_0) = 90^\circ$. The initial Greenwich hour angle of the vernal equinox $A_\Upsilon(t_0) = 59.03^\circ$. The designed kinematic parameters vary as shown in Figure 17.

The simulation parameters of various navigational apparatus are shown in Table 2. In addition, $\alpha_s = 70^\circ$, $\alpha_A = 1.009$, FOV $3^\circ \times 3^\circ$ and $\delta v_{E,N,U}(t_0) = 0.1$ m/s, $\Phi_{x,y,z}(t_0) = 1''$, $\delta\varphi(t_0) = \delta\lambda(t_0) = 1''$, $\delta h(t_0) = 50$ m.

5.3.2. Flight simulation within 4 h

In one 4 h flight cycle, the constant $M = 8.0$. For the proposed deep integrated method with refraction corrected and the traditional method with refraction uncorrected, the real-time simulation errors of navigation parameters are estimated as shown in Figures 18–21. The RMSEs of the navigation parameters are shown in Table 3.

Table 2. Simulation parameters of navigational apparatus.

Apparatus	Precision	Sampling period
Gyroscope	constant drift $0.01^\circ/h$, random drift $0.005^\circ/h$ (1σ)	0.1 s
Accelerometer	constant bias $10 \mu g$, random bias $5 \mu g$ (1σ)	0.1 s
Star sensor	measurement error $2''$ (1σ)	0.5 s

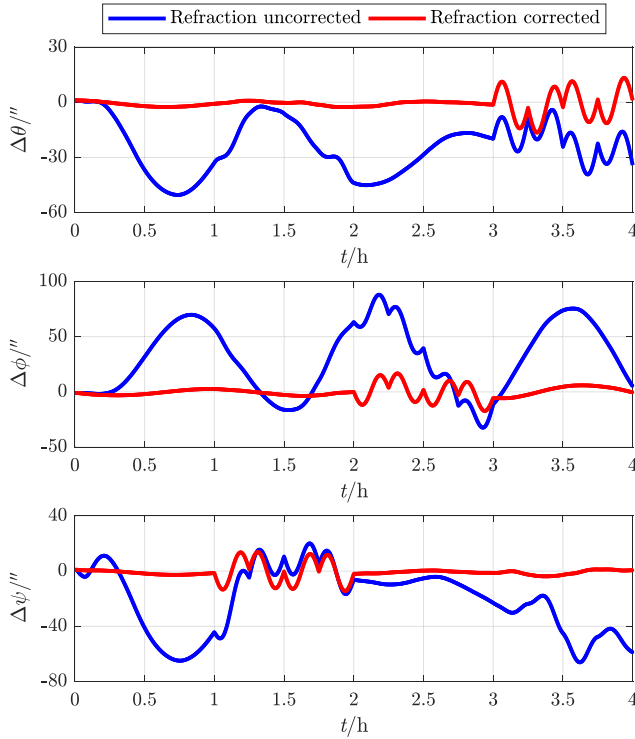


Figure 18. Attitude error within 4 h.

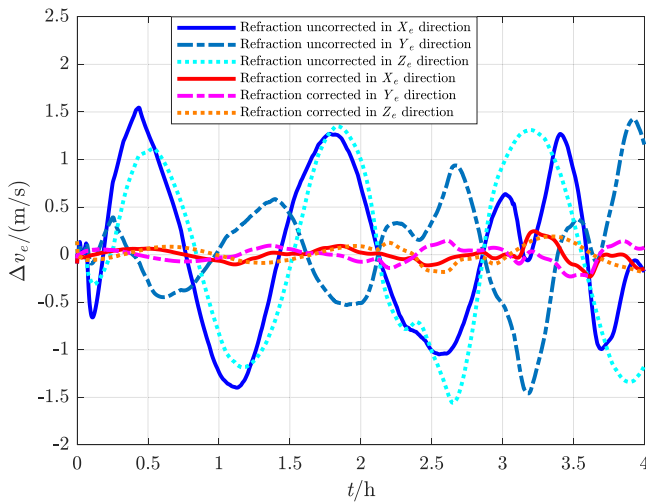


Figure 19. Velocity error within 4 h.

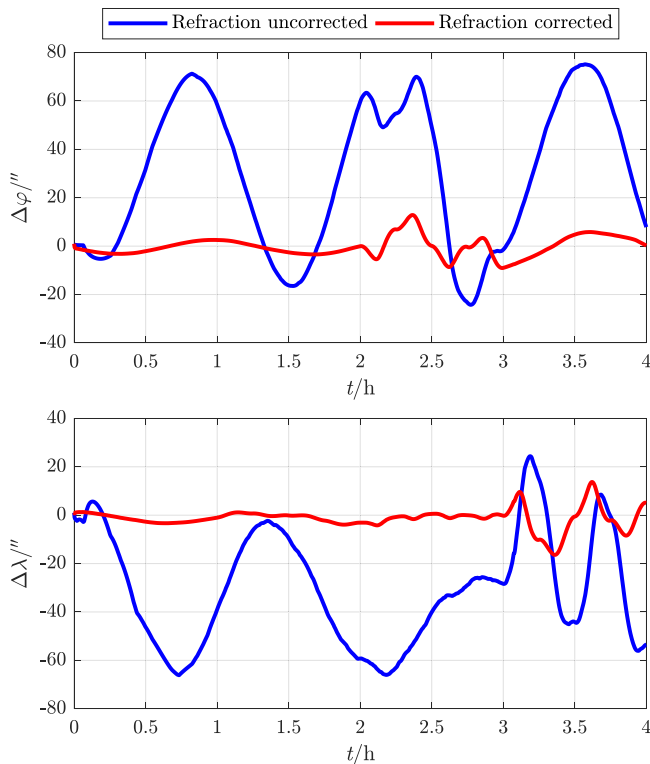


Figure 20. Geographical coordinate error within 4 h.

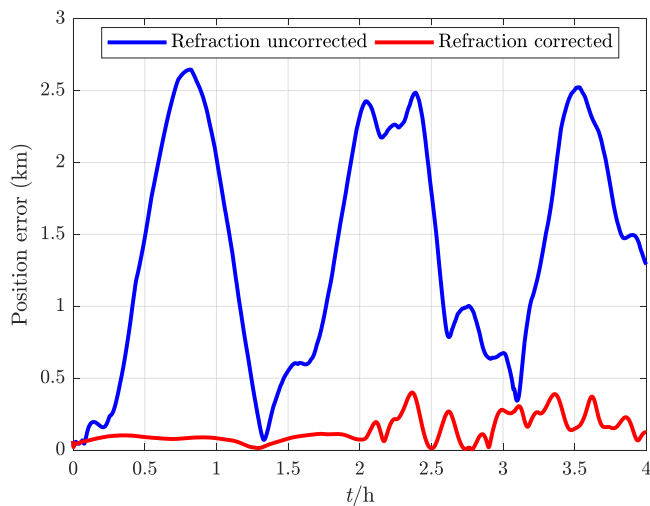


Figure 21. Total position error within 4 h.

Table 3. Navigation parameter RMSE of 4 h flight.

	Refraction uncorrected	Refraction corrected
$(\Delta\theta, \Delta\phi, \Delta\psi)''$	(28.07, 43.95, 31.59)	(4.59, 5.45, 4.89)
$(\Delta v_{ex}, \Delta v_{ey}, \Delta v_{ez})/(m/s)$	(0.82, 0.55, 0.90)	(0.08, 0.08, 0.09)
$(\Delta\varphi, \Delta\lambda)''$	(42.72, 38.31)	(4.07, 4.32)
Total position error (m)	1604	162

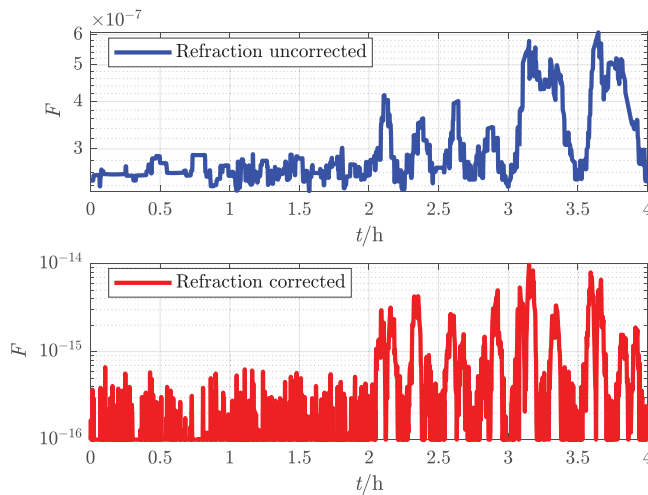


Figure 22. Loss function within 4 h.

It can be seen that, under the influence of atmospheric refraction, all the navigation error data of the traditional integrated method without correction oscillate or even diverge, while the proposed deep integrated method with correction can eliminate the influence of tight coupling between attitude and position on navigation accuracy, and thus effectively restrain navigation error within a limited range even in manoeuvring flight.

The real-time loss functions of the two methods are plotted in Figure 22. Although the orders of magnitude are so small that the numerical value may overflow in calculation, it does verify that smaller function value indicates higher navigation accuracy.

5.3.3. Flight simulation within 24 h

For the purpose of simulating the decrease of limiting magnitude with enhancing atmospheric background radiation in long-endurance flight, M is respectively set to 8.0, 7.7, 7.4, 7.1, 6.8 and 6.5 in six continuous flight cycles (i.e., 24 h flight). The final results of the proposed deep integrated method are shown in Figure 23.

It can be seen that, with the decrease of limiting magnitude together with the number of observed stars among different flight cycles, the navigation accuracy tends to be worse. Nevertheless, the position RMSE in each hour can still be restrained within 1.5 km and the attitude real-time error can be restrained within 70'' even after 24 h manoeuvring flight with limiting magnitude above 6.5. Obviously, the proposed method can overcome the problem of unreliability of CNS operating by itself. When better conditions are satisfied, e.g., all the sensors are available to detect stars all the time, higher navigation accuracy can be achieved, and thus the cruising ability of the UAV can be ensured.

6. Conclusions

- (1) Based on the atmospheric refraction model, the introduction of a stellar azimuth coordinate system can help to effectively establish the coupling relationship between attitude parameters and position parameters.
- (2) Based on the geometric relationship whereby all the stellar azimuth planes intersect on the common zenith direction, the proposed loss function can be utilised to evaluate the navigation accuracy. This can be also applicable to further intelligent navigation algorithms.
- (3) The observed refracted starlight with wider zenith distance contributes to precise positioning, while the observed refracted starlight with narrower zenith distance contributes to precise attitude determination. Therefore, the strapdown installation of triple-FOV CNS must comprehensively

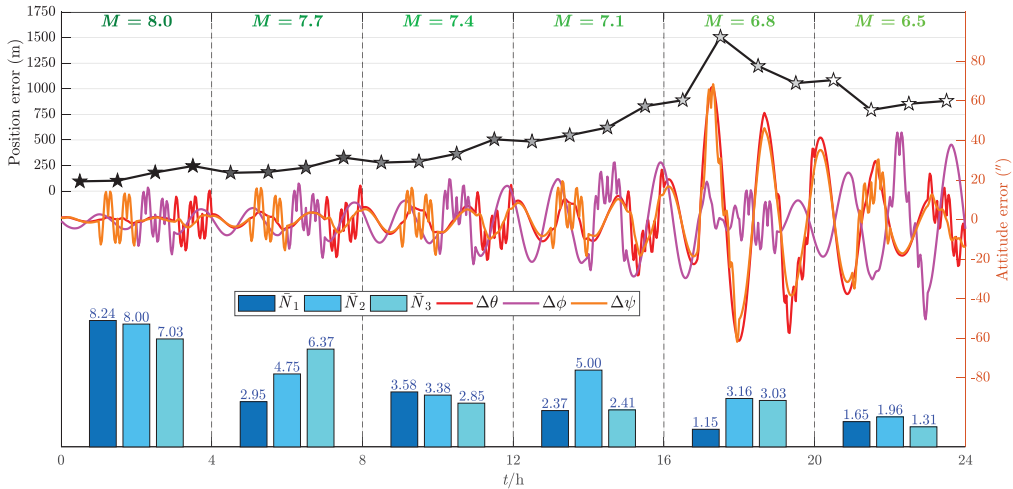


Figure 23. Navigation error and mean number of observed stars within 24 h.

coordinate the position accuracy, attitude accuracy, application range of atmospheric refraction model and the manoeuvring flight strategy according to the engineering requirements.

- (4) CNS alone cannot ensure sufficient position accuracy by a rough attitude with refraction influence, which is unacceptable for an aerial vehicle.
- (5) The SIMU/triple star sensors deep integrated method can correct the attitude error through the atmospheric refraction model as well as a rough location and horizontal reference provided by SINS, acquiring a more accurate position. Based on the high-precision daytime star sensors with strong detectivity, this method can ensure navigation accuracy by Kalman filter even for all-day flight, which can be applicable to a HALE UAV in steady-state cruise in the stratosphere.

Refractivity in the stratosphere is weaker than at sea level, so the precise refraction model and horizontal reference are strictly demanded. When adjusting the refraction model for some specific complex circumstances, the methodology proposed in this paper also applies. In addition, the acquisition of precise altitude information and the evasion of the sun or the moon should be seriously considered in engineering applications.

Acknowledgements. This research is supported by the Defense Industrial Technology Development Program under research grant JCKY2018601B101, which is greatly appreciated.

References

- Chapman, D., Aboobaker, A. M., Araujo, D., Didier, J., Grainger, W., Hanany, S., Hillbrand, S., Limon, M., Miller, A., Reichborn-Kjennerud, B., Sagiv, I., Tucker, G. and Vinokurov, Y. (2015). Star Camera System and New Software for Autonomous and Robust Operation in Long Duration Flights. *Aerospace Conference IEEE*, Big Sky, MT, 1–11.
- Fan, Q. and Li, X. (2011). Selection of optical-system parameters for an all-day used star sensor. *Acta Optica Sinica*, **31**(11), 254–260.
- He, Z., Wang, X. and Fang, J. (2014). An innovative high-precision SINS/CNS deep integrated navigation scheme for the Mars rover. *Aerospace Science & Technology*, **39**, 559–566.
- Ho, K. (2012). A survey of algorithms for star identification with low-cost star trackers. *Acta Astronautica*, **73**, 156–163.
- Honda, M., Athar, M. S., Kajita, T., Kasahara, K. and Midorikawa, S. (2015). Atmospheric neutrino flux calculation using the NRLMSISE-00 atmospheric model. *Physical Review D*, **92**(2), 023004.
- Kurzke, J. and Halliwell, I. (2018). Gas Properties and Standard Atmosphere. In: *Propulsion and Power. An Exploration of Gas Turbine Performance Modeling*. Cham: Springer, 613–618.
- Li, B., Sun, Q. and Zhang, T. (2015). A star pattern recognition algorithm for the double-FOV star sensor. *IEEE Aerospace & Electronic Systems Magazine*, **30**(8), 24–31.

- Li, P., Sheng, G., Zhang, X., Wu, J., Xu, B., Liu, X. and Zhang, Y. (2018). Underwater terrain-aided navigation system based on combination matching algorithm. *ISA Transactions*, **78**, 80–87.
- Liu, J., Feng, Y. and Zou, L. (2018). Some three-term conjugate gradient methods with the inexact line search condition. *Calcolo*, **55**(2), 16.
- Ning, X. and Wang, L. (2013). Method of high accuracy celestial altitude obtainment in vessel navigation. *Acta Optica Sinica*, **33**(3), 17–25.
- Ning, X., Zhang, J., Gui, M. and Fang, J. (2018). A fast calibration method of the star sensor installation error based on observability analysis for the tightly coupled SINS/CNS integrated navigation system. *IEEE Sensors Journal*, **18**(16), 6794–6803.
- Nocedal, J. and Wright, S. J. (2006). *Numerical Optimization*. New York: Springer.
- Pan, Q., Cheng, Y., Liang, Y., Yang, F. and Wang, X. (2013). *Multi-Source Information Fusion Theory and Its Applications*. Beijing: Tsinghua University Press.
- Qin, Y. (2006). *Inertial Navigation*. Beijing: Science Press.
- Rex, M., Chapin, E., Devlin, M. J., Gundersen, J., Klein, J., Pascale, E. and Wiebe, D. (2006). BLAST autonomous daytime star cameras. *Proceedings of SPIE - The International Society for Optical Engineering*, **6269**, 1–8.
- Rivaie, M., Mamat, M. and Abashar, A. (2015). A new class of nonlinear conjugate gradient coefficients with exact and inexact line searches. *Applied Mathematics and Computation*, **268**, 1152–1163.
- Shuster, M. D. and Oh, S. D. (1981). Three-axis attitude determination from vector observations. *Journal of Guidance and Control*, **4**(1), 70–77.
- The Purple Mountain Observatory, Chinese Academy of Sciences. (2021). *Chinese Astronomical Almanac 2021*. Beijing: Science Press.
- Wang, H., Lin, H. and Zhou, W. (2011). Technology of atmospheric refraction compensation in starlight observation. *Acta Optica Sinica*, **31**(11), 7–12.
- Wang, K., Zhu, T., Qin, Y., Zhang, C. and Li, Y. (2017a). Integration of star and inertial sensors for spacecraft attitude determination. *Journal of Navigation*, **70**(6), 1–14.
- Wang, W., Wei, X., Li, J. and Wang, G. (2017b). Noise suppression algorithm of short-wave infrared star image for daytime star sensor. *Infrared Physics & Technology*, **85**, 382–394.
- Wang, H., Gao, Z. and Wang, K. (2021a). An accuracy evaluation method of stellar navigation for aircraft based on atmospheric refraction. Chinese Patent, 202110176450.6.
- Wang, H., Hua, W., Xu, H. and Xu, Y. (2021b). Centroiding method for star image spots under interference of Sun straylight noise in a star sensor. *Acta Optica Sinica*, **41**(03), 143–151.
- Wu, L., Wang, J. and Wang, H. (2015). Guide star selection for star pattern recognition between three FOVs. *Optics & Precision Engineering*, **23**(6), 1732–1741.
- Wu, L., Xu, Q., Wang, H., Lyu, H. and Li, K. (2019). Guide star selection for the three-FOV daytime star sensor. *Sensors*, **19**(6), 1457.
- Yu, Y., Cao, J., Tang, Z., Luo, H. and Zhao, M. (2015). Differential measurement of atmospheric refraction using a telescope with double fields of view. *Research in Astronomy and Astrophysics*, **15**(10), 1742–1750.
- Zheng, X., Huang, Y., Mao, X., He, F. and Ye, Z. (2020). Research Status and Key Technologies of All-day Star Sensor. *Journal of Physics Conference Series - 2019 The 10th Asia Conference on Mechanical and Aerospace Engineering*, **1510**, 012027.
- Zhu, X., Ma, M., Cheng, D. and Zhou, Z. (2017). An optimized triad algorithm for attitude determination. *Artificial Satellites*, **52**(3), 41–47.
- Zhu, J., Wang, X., Li, H., Che, H. and Li, Q. (2018). A high-accuracy SINS/CNS integrated navigation scheme based on overall optimal correction. *Journal of Navigation*, **71**, 1567–1588.

Appendix

For Equation (25), according to the Jacobi identity in elliptic function theory, assign

$$\mathbf{J} = \zeta_b \times (\mathbf{v}_a \times \mathbf{v}_r) + \mathbf{v}_a \times (\mathbf{v}_r \times \zeta_b) + \mathbf{v}_r \times (\zeta_b \times \mathbf{v}_a) = 0 \quad (\text{A1})$$

Therefore,

$$\begin{aligned} (\mathbf{v}_a \times \mathbf{v}_r) \times \mathbf{J} \cdot \zeta_b &= (\mathbf{v}_a \times \mathbf{v}_r) \times [\zeta_b \times (\mathbf{v}_a \times \mathbf{v}_r)] \cdot \zeta_b + (\mathbf{v}_a \times \mathbf{v}_r) \times [\mathbf{v}_a \times (\mathbf{v}_r \times \zeta_b)] \cdot \zeta_b \\ &\quad + (\mathbf{v}_a \times \mathbf{v}_r) \times [\mathbf{v}_r \times (\zeta_b \times \mathbf{v}_a)] \cdot \zeta_b = 0 \end{aligned} \quad (\text{A2})$$

As \mathbf{v}_a , \mathbf{v}_r and ζ_b are unit vectors, thus

$$\begin{aligned} (\mathbf{v}_a \times \mathbf{v}_r) \times [\zeta_b \times (\mathbf{v}_a \times \mathbf{v}_r)] \cdot \zeta_b &= \zeta_b \cdot [(\mathbf{v}_a \times \mathbf{v}_r) \cdot (\mathbf{v}_a \times \mathbf{v}_r)] \cdot \zeta_b - (\mathbf{v}_a \times \mathbf{v}_r) \cdot [(\mathbf{v}_a \times \mathbf{v}_r) \cdot \zeta_b] \cdot \zeta_b \\ &= [\mathbf{v}_r \times (\mathbf{v}_a \times \mathbf{v}_r) \cdot \mathbf{v}_a] \cdot \zeta_b^2 - [(\mathbf{v}_a \times \mathbf{v}_r) \cdot \zeta_b]^2 \\ &= [\mathbf{v}_a \cdot (\mathbf{v}_r \cdot \mathbf{v}_r) \cdot \mathbf{v}_a - \mathbf{v}_r \cdot (\mathbf{v}_r \cdot \mathbf{v}_a) \cdot \mathbf{v}_a] \cdot \zeta_b^2 - [(\mathbf{v}_a \times \mathbf{v}_r) \cdot \zeta_b]^2 \\ &= 1 - (\mathbf{v}_r \cdot \mathbf{v}_a)^2 - [(\mathbf{v}_a \times \mathbf{v}_r) \cdot \zeta_b]^2 \end{aligned} \quad (\text{A3})$$

$$\begin{aligned} (\mathbf{v}_a \times \mathbf{v}_r) \times [\mathbf{v}_a \times (\mathbf{v}_r \times \zeta_b)] \cdot \zeta_b &= \mathbf{v}_a \cdot [(\mathbf{v}_a \times \mathbf{v}_r) \cdot (\mathbf{v}_r \times \zeta_b)] \cdot \zeta_b - (\mathbf{v}_r \times \zeta_b) \cdot [(\mathbf{v}_a \times \mathbf{v}_r) \cdot \mathbf{v}_a] \cdot \zeta_b \\ &= \mathbf{v}_a \cdot [\mathbf{v}_r \times (\mathbf{v}_r \times \zeta_b) \cdot \mathbf{v}_a] \cdot \zeta_b - [(\mathbf{v}_a \times \mathbf{v}_r) \cdot \mathbf{v}_a] \cdot (\mathbf{v}_r \times \zeta_b) \cdot \zeta_b \\ &= \mathbf{v}_a \cdot [\mathbf{v}_r \cdot (\mathbf{v}_r \cdot \zeta_b) \cdot \mathbf{v}_a - \zeta_b \cdot (\mathbf{v}_r \cdot \mathbf{v}_r) \cdot \mathbf{v}_a] \cdot \zeta_b \\ &= (\mathbf{v}_r \cdot \zeta_b) \cdot (\mathbf{v}_r \cdot \mathbf{v}_a) \cdot (\mathbf{v}_a \cdot \zeta_b) - (\zeta_b \cdot \mathbf{v}_a)^2 \end{aligned} \quad (\text{A4})$$

$$\begin{aligned} (\mathbf{v}_a \times \mathbf{v}_r) \times [\mathbf{v}_r \times (\zeta_b \times \mathbf{v}_a)] \cdot \zeta_b &= \mathbf{v}_r \cdot [(\mathbf{v}_a \times \mathbf{v}_r) \cdot (\zeta_b \times \mathbf{v}_a)] \cdot \zeta_b - (\zeta_b \times \mathbf{v}_a) \cdot [(\mathbf{v}_a \times \mathbf{v}_r) \cdot \mathbf{v}_r] \cdot \zeta_b \\ &= \mathbf{v}_r \cdot [\mathbf{v}_r \times (\zeta_b \times \mathbf{v}_a) \cdot \mathbf{v}_a] \cdot \zeta_b \\ &= \mathbf{v}_r \cdot [\zeta_b \cdot (\mathbf{v}_r \cdot \mathbf{v}_a) \cdot \mathbf{v}_a - \mathbf{v}_a \cdot (\mathbf{v}_r \cdot \zeta_b) \cdot \mathbf{v}_a] \cdot \zeta_b \\ &= (\mathbf{v}_r \cdot \mathbf{v}_a) \cdot (\zeta_b \cdot \mathbf{v}_a) \cdot (\mathbf{v}_r \cdot \zeta_b) - (\mathbf{v}_r \cdot \zeta_b)^2 \end{aligned} \quad (\text{A5})$$

Therefore,

$$(\mathbf{v}_a \times \mathbf{v}_r \cdot \zeta_b)^2 = 1 - (\mathbf{v}_a \cdot \mathbf{v}_r)^2 - (\mathbf{v}_r \cdot \zeta_b)^2 - (\zeta_b \cdot \mathbf{v}_a)^2 + 2(\mathbf{v}_a \cdot \mathbf{v}_r)(\mathbf{v}_r \cdot \zeta_b)(\zeta_b \cdot \mathbf{v}_a) \quad (\text{A6})$$

As \mathbf{v}_a , \mathbf{v}_r and ζ_b are coplanar, thus

$$(\mathbf{v}_a \times \mathbf{v}_r \cdot \zeta_b)^2 = 1 - (\mathbf{v}_a \cdot \mathbf{v}_r)^2 - (\mathbf{v}_r \cdot \zeta_b)^2 - (\zeta_b \cdot \mathbf{v}_a)^2 + 2(\mathbf{v}_a \cdot \mathbf{v}_r)(\mathbf{v}_r \cdot \zeta_b)(\zeta_b \cdot \mathbf{v}_a) = 0 \quad (\text{A7})$$